



Supplementary Information for
Anatomy of Strike Slip Fault Tsunami-genesis

Ahmed Elbanna, Mohamed Abdelmeguid, Xiao Ma, Faisal Amlani, Harsha. S. Bhat, Costas Synolakis, Ares J. Rosakis

Ares J. Rosakis
Email: arosakis@caltech.edu

This PDF file includes:

Supplementary text
Figures S1 to S8
Table S1
SI References

Supplementary Information Text

S1. Earthquake Model Setup

The earthquake is initiated on a vertically dipping planar fault located at $x_2 = 0$ within a 3D simulation domain spanning $(x_1, x_2, x_3) \in (-10, 60) \times (-15, 15) \times (-0.7, -15.7)$ km. The origin of the coordinate system is located at the initially undisturbed sea surface level positioned 700 m above the sea floor level in the middle of the bay. The linear elasto-dynamics is described by a system of time-dependent field equations subject to suitable initial and boundary conditions related to a body transmitting elastic waves. The governing equations are given by:

$$\sigma_{ij,j} + b_i = \rho \ddot{u}_i \quad (1)$$

Where, σ_{ij} correspond to the stress tensor, b_i are the body forces, and \ddot{u}_i is the second time derivative of the displacement field. For a linear isotropic material, the constitutive relation becomes:

$$\sigma_{ij} = \lambda \delta_{ij} \varepsilon_{kk} + 2\mu \varepsilon_{ij} \quad (2)$$

where ε_{ij} is the strain tensor, and μ , and λ are the Lamé parameters. The constitutive parameters are given in Table S1. In the limit of small deformations, the strain field is expressed in terms of the displacement field u_i as follows:

$$\varepsilon_{ij} = \frac{1}{2} [u_{i,j} + u_{j,i}] \quad (3)$$

The fault slippage is governed by a linear slip-weakening friction model. The shear tractions T_f is described in terms of slip d , and fault normal traction T_n as:

$$T_f = \begin{cases} -[\mu_s - (\mu_s - \mu_d)d/d_o]T_n & \text{for } d \leq d_o \text{ and } T_n \leq 0 \\ -\mu_d T_n & \text{for } d > d_o \text{ and } T_n \leq 0 \end{cases} \quad (4)$$

Here, μ_s is the static coefficient of friction, μ_d is the dynamic coefficient of friction, and d_o is the characteristic slip-weakening distance. The frictional properties are distributed along the depth, such that there is locked-slipping interface located at $x_3 = -11.7$ km. No slip is allowed below the locked-slipping boundary (i.e., for $x_3 < -11.7$ km). Fig. S6 demonstrates the relationship between the shear stress and the slip for the prescribed linear slip-weakening law.

As mentioned in Earthquake Model section, the transition from sub-Rayleigh rupture to supershear is governed by strength parameter S^* defined as:

$$S^* = \frac{T_s - T_o}{T_o - T_d} \quad (5)$$

Here, T_s is the static shear strength, T_o is the initial shear stress, and T_d is the dynamic shear strength. For planar faults in unbounded 3D linear elastic homogeneous media, with no free surface, Dunham (2007) showed analytically and numerically that there exists a maximum value of S^* , given by $S^* = 1.19$, beyond which transition to supershear rupture propagation is not possible (2). The presence of the free surface may alter this threshold and enables transition at higher S^* value (3). The sustainability of the supershear transition, induced by the free surface, depends on many factors including normal stress variation, as highlighted recently by Hu et al (4).

For the supershear rupture case, the fault frictional parameters above the locked-slipping boundary are $\mu_s = 0.6$ and $\mu_d = 0.3$ for the static and dynamic friction coefficients, respectively, and $d_o = 0.2$ for the slip-weakening distance. The stress is initially distributed over the fault surface as $T_n = -50$ MPa, and $T_o = 24$ MPa. The static shear strength is $T_s = \mu_s |T_n| = 0.6 * 50 = 30$ MPa. The dynamic shear strength is $T_d = \mu_d |T_n| = 0.3 * 50 = 15$ MPa. For these parameters, the dynamic stress drop for the supershear case is equal to $\Delta T = T_o - T_d = 9$ MPa. However, the shear stress is locally increased within an overstressed region to a value of $T_o = 31$ MPa to forcefully start the rupture. The overstressed region is a square patch centered at the

hypocenter located at $(x_1, x_2, x_3) = (0, 0, -6.7)$ km on the fault surface and have dimensions of (1.8×1.8) km. The fault stresses and properties outside the overstressed region correspond to a strength parameter $S^* = 0.667$.

For the sub-Rayleigh rupture case, the fault frictional parameters above the locked-slipping boundary are identical to those in the supershear case. However, the fault shear stress is initially distributed to have a value $T_o = 31$ MPa within the overstressed patch, and a value of $T_o = 19.2$ MPa outside the overstressed region, respectively. The normal compressive stress is uniform throughout and is equal to $T_n = -50$ MPa, identical to the supershear case. This corresponds to a dynamic stress drop of $\Delta T = 4.2$ MPa. In this case, the fault stresses and properties outside the overstressed region correspond to a strength parameter $S^* = 2.62$. The higher value of the S^* parameter favors sub-Rayleigh rupture propagation and significantly delay the supershear transition, if it is to occur due to the free-surface effect.

In our dynamic rupture simulations, we discretized the domain using 216 million hexahedral elements with an element size of $50 \times 50 \times 50$ m. The choice of the element size is such that the process zone, which is the fundamental elasto-frictional length scale in our problem, is well resolved. A more detailed discussion for the process zone size for slip-weakening friction law is found in Equations 30a and 33 from Day et. al. 2005 (1). We have computed this length scale using the frictional parameters in our study and found it to be equal to 380 m. Day et al. (2005) recommended using 3-5 spatial cells to resolve this critical length scale. We opted for higher resolution and used an element size of 50 m. This discretization level resolves the critical length scale with 7-8 elements. The process zone size decreases as the rupture speed increases, as noted in Day et. al. (2005). We have estimated the minimum value of the process zone size in our simulation to be around 228 m. With our current element size of 50 m, the minimum process zone is resolved with 4-5 elements. Temporally, we have used an explicit forward Euler time integration with time step controlled by the CFL condition. Specifically, the time step in the dynamic rupture simulations corresponds to half the CFL bound: $\Delta t = 0.5 \times \Delta t_{CFL} = 0.5 \times \Delta x / c_{p_2}$ where c_p is the dilatational (pressure) wave speed in the solid crust.

S2. Tsunami Model Setup

For the tsunami modelling, we consider the nonlinear shallow water wave approximation for incompressible flow with constant density ρ in a domain $\Omega \in R^2$ governed by Eq.1 in the main text for $\forall t \in [0, T]$, where T is the tsunami total simulation time. A Cartesian coordinate system is chosen such that $x_3 = 0$ corresponds to the undisturbed water level. The epicenter of the earthquake is located at $(x_1, x_2, x_3) = (0, 0, -0.7)$ km. For the tsunami model the domain of the problem is defined by $(x_1, x_2) \in (0, L) \times (-W/2, W/2)$, where L and W are the length and width of the simulation domain, respectively. The discretization of the tsunami domain is independent of the solid domain, and a uniform mesh with element size 12.5 m was used in the spatial discretization. Temporally, the solution of the shallow water equations evolves at a different time scale from the dynamic rupture. We thus allow, within our unconditionally stable MOOSE-SWIM implicit Euler solver, for a different time step in the tsunami model, constrained by the accuracy requirements. We have also run the simulations at different time resolutions to check for convergence.

The following boundary conditions were imposed on the shallow water equations (Eq.1 in the main text):

$$\begin{aligned}
 \hat{v}_1(x_1 = L, x_2, t) &= 0 \\
 \hat{v}_2(x_1, x_2 = W/2, t) &= \hat{v}_2(x_1, x_2 = -W/2, t) = 0 \\
 h_{,2}|_{W/2} &= h_{,2}|_{-W/2} = 0 \\
 h_{,1}|_L &= 0
 \end{aligned} \tag{6}$$

The undeformed bathymetry that is used in our tsunami model is sketched in Fig. 2a in the main text and is shown in detail in Fig. S7. This bathymetry is given by $H_o(x_i) = a + (b - a)F_o(x_i)$, where F_o is a hyperbolic tangent function defined by the following equation:

$$F_o = \begin{cases} \frac{1}{2} \left(1 - \tanh \frac{r-r_c}{w} \right) & \text{for } x_1 \geq c \\ \frac{1}{2} \left(1 - \tanh \frac{|x_2|-r_c}{w} \right) & \text{for } x_1 \leq c \end{cases} \quad (7)$$

Here, a, b are the minimum and maximum depth respectively, r is given by $\sqrt{(x_1^2 + x_2^2)}$. This represents the radial distance measured from the center of the semi-circular apex region. r_c is the specified mean radius of the apex region, c is the center point of the apex of the bay and w is a constant that defines the slope of the bay. We choose this generic bathymetry to decouple our conclusions from any effect of shoreline geometric complexity that may mask tsunami dynamics.

The choice of the 2-D domain and bathymetry shown in Fig. S7 for the tsunami model has been motivated by the Palu Bay in which the bay depth varies from 700 m at the center to 10 m near the coast. We acknowledge, however, that the bathymetry of the Palu Bay is more complex and includes multiscale features that are absent in the generic bay geometry presented here. In our analysis we opted for a more generic bathymetry to focus our attention on basic tsunami generation processes that would, otherwise, be obscured by more complex bathymetries.

The simulated domain has the following dimensions $L = 37$ km and $W = 5$ km. For the bay bathymetry we have assumed the following parameters: minimum depth $a = 10$ m, maximum depth $b = 700$ m, mean radius of the apex $r_c = 3$ km, location of the apex center $c = 30.5$ km, and slope parameter $w = 400$. This specific choice of this slope parameter w results in a slope varying from 700 m to 10 m over to a 2 km distance. We note that the three-dimensional earthquake model assumes a flat free surface. The resultant free surface displacement is then mapped to the prescribed bathymetry.

We study the convergence of our SWIM code for the tsunami generated by the supershear rupture scenario. In the convergence study, we considered meshes of 50 m, 25 m, and 12.5 m element size and compared the time histories of the water level amplitude at the four different stations OP-1, OP-2, OP-3 and OP-4. As shown in Fig. S5, we observe that as we refine the mesh, the solutions at stations OP-1, OP-3 and OP-4 are identical for the meshes of 25 m and 12.5 m element size. Furthermore, the amplitude and wavelength of the trailing oscillations observed in the time history at OP-2 are reduced when the mesh is refined. However, the peak amplitudes and wave arrival times do not change.

S3. SWIM Verification

To validate our SWIM implementation, we solve the nonlinear shallow water equation (NSWE) for the "piston" motion problem described in Derakhti et al. (2019) (5). Derakhti et al. (2019) used the Smooth Particle Hydrodynamics (SPH) method of Dalrymple and Rogers (2006) (6), and validated their results using experimental data from Hammack (1973) (7). For reference, our SWIM code solves the NSWE in an incompressible inviscid domain assuming depth-averaged variables. The validation against the SPH method and the laboratory results allows for checking the veracity of SWIM and the adequacy of the NSWE approximation, particularly when gauging the influence of a dynamically moving seabed.

We solve the 1D nonlinear shallow water equation with identical geometry to the domain setup in the x-z plane as in Derakhti et al. (2019). The seafloor displacement $u_3^s(t)$ is given as:

$$u_3^s(x_1, t) = \begin{cases} 0 & \text{for } t < 0 \\ \frac{1}{2} U_m \left[1 - \cos \frac{\pi t}{t_r} \right] \mathcal{H}(b_o^2 - x_1^2) & \text{for } 0 \leq t \leq t_r \\ U_m \mathcal{H}(b_o^2 - x_1^2) & \text{for } t > t_r \end{cases} \quad (8)$$

Here, the ocean depth is H . A portion of the sea floor with half width b_o is displaced upward for a total distance U_m over the rise time t_r . The width of the seafloor displacement is imposed through \mathcal{H} the Heaviside step function. Following Derakhti et al. (2019), a number of dimensionless quantities are introduced to define the loading rate, namely, $t_c = b_o / \sqrt{gH}$, and $\tau = t_r / t_c$. Note that for a similar setup, a lower τ indicates a smaller rise time t_r .

To explore the impact of the loading rate, we compare two cases with the numerical solution from Derakhti et al. (2019) and the experimental results from Hammack (1973): (1)

Impulsive loading with $\tau = 0.11$ and $U_m/H = 0.4$, (2) Transitional loading with $\tau = 0.9$ and $U_m/H = 0.01$. Fig. S8a illustrate the different normalized sea surface displacement h/U_m at $x_1/b_o = 0$ corresponding to the center of the seafloor. The shallow water equation compares well in terms of maximum amplitude as well as the trailing wave behavior. Fig. S8b demonstrates better agreement for the far edge of seafloor displacement at $x_1/b_o = 1$.

For case (2) with transitional loading, we observe deviations in the peak amplitude at the center of the seafloor displacement, as shown in Fig. S8c. This discrepancy is attributed to the low U_m/H parameter, indicating further deviation from the shallow water limit. Similarly, the results further away from the center of the seafloor displacement show better agreement, as illustrated in Fig.S8d.

Furthermore, lack of oscillations is observed in the shallow water solution when compared with SPH and experimental observations. This is attributed to the nature of the depth-averaging approximation of the shallow water wave equation. Such absence was also reported in Stefanakis et al. (2015) (8), who provided analytic solutions for the rise of a sill off the seafloor. Overall, the major features of the solution are still preserved, such as the rise time, peak amplitude, and approach to steady state.

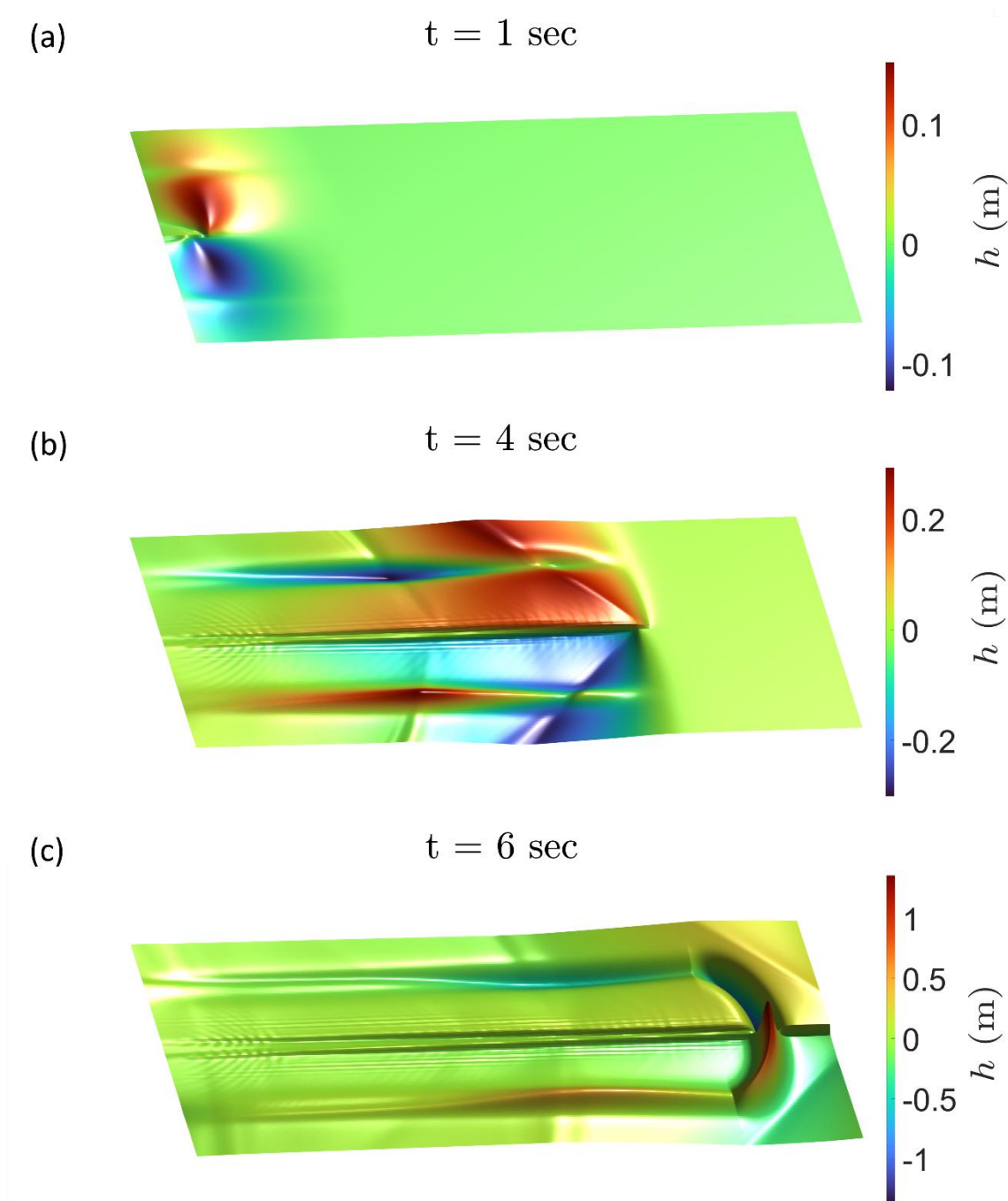


Fig. S1. Evolution of the earthquake-induced tsunami in a bay traversed by a supershear rupture. (a-c) Snapshots of the supershear tsunami scenario at 1, 4, and 6 s, shown sequentially from top to bottom. Colors indicate the sea surface height h relative to the undisturbed water level. These snapshots correspond to the “dynamic tsunami generation phase” shown in Fig. 2 (a)-(c) in the main text with the main difference that here the scale bar is adjusted according to the sea surface peak height in each subplot

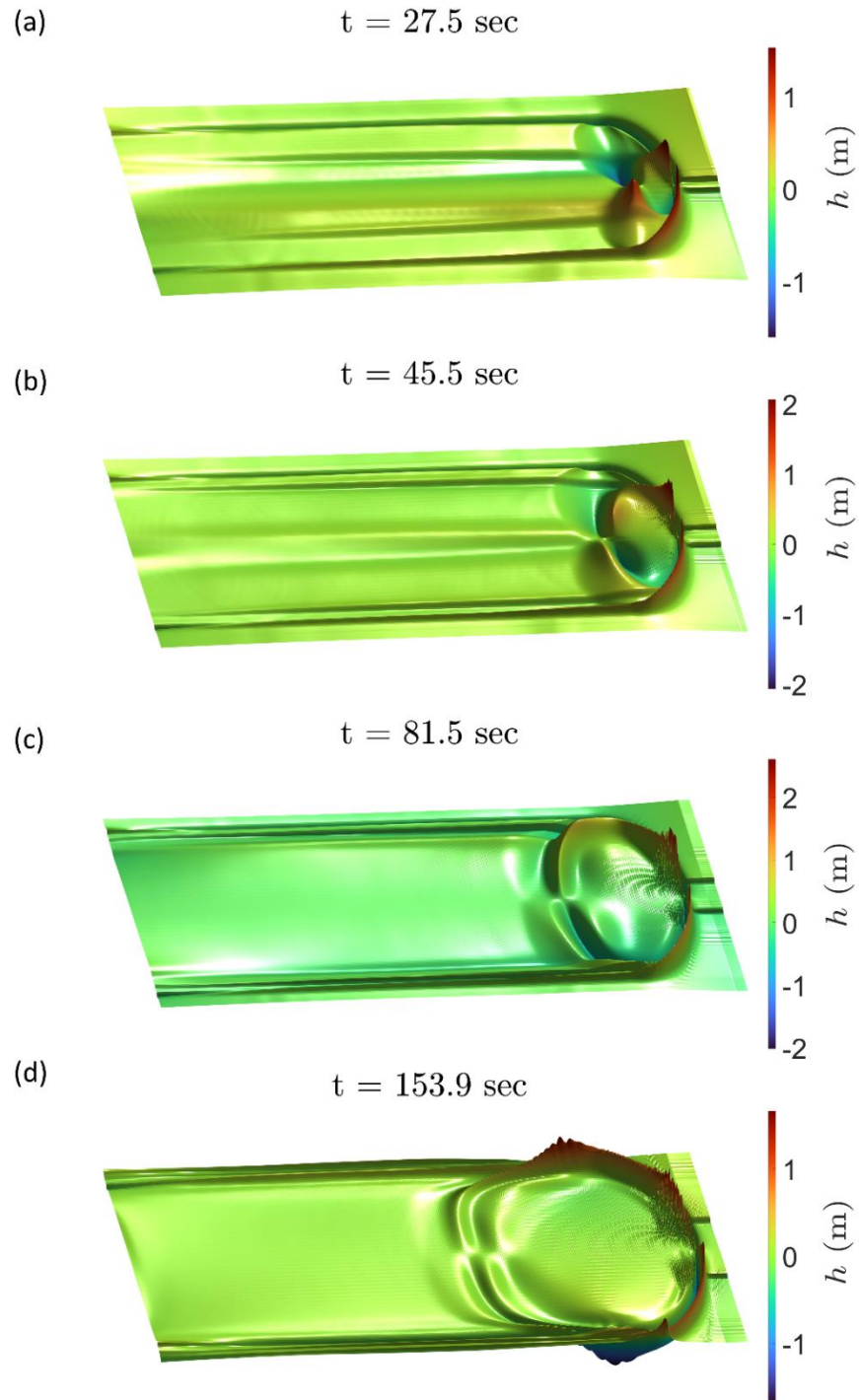


Fig. S2. Evolution of the earthquake induced tsunami in a bay traversed by a supershear rupture. (a-d) Snapshots of the supershear tsunami scenario at 27.5, 45.5, 81.5 and 153.9 s, shown sequentially from top to bottom. Colors indicate the sea surface height h relative to the undisturbed water level. These snapshots correspond to the “post-seismic tsunami generation phase” shown in Fig. 2 (d)-(f) in the main text, with the main difference that here the scale bar is adjusted according to the sea surface peak height in each subplot

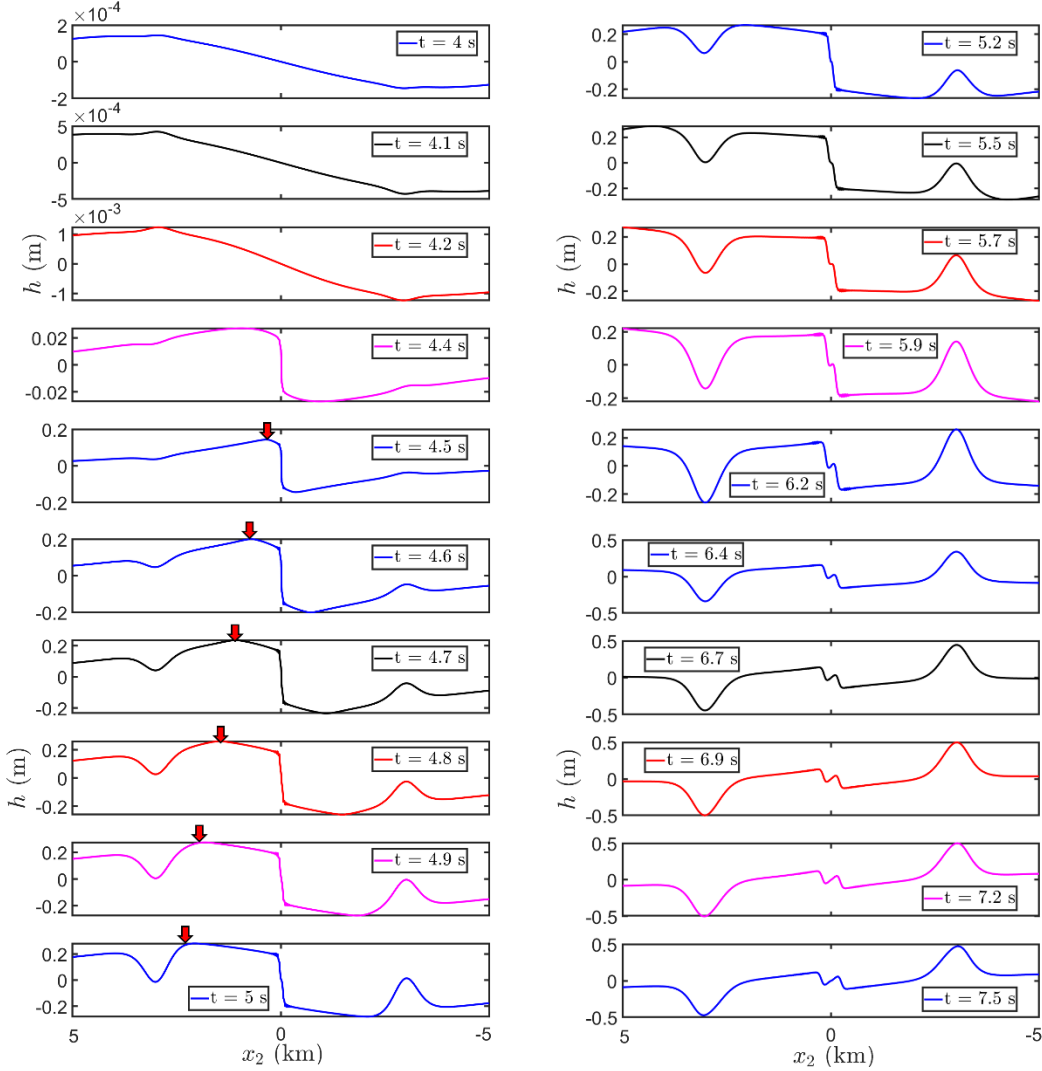


Fig. S3. Snapshots of sea surface height h for cross section A-A during the dynamic tsunami phase. The snapshots capture, in more detail, the evolution of the dynamic tsunami generation phase between times $t = 4.0$ s, and $t = 7.5$ s. The height scale varies according to the sea surface peak height at each displayed time. Between times $t = 4.0$ s and $t = 4.4$ s, the sea surface is perturbed by the dilatational wave field which propagates ahead of the rupture front and precedes the arrival of the shear shock wave fronts. The lack of any vertical displacement at $x_2 = 0$ in the subplots for times $t = 4.0$ s, 4.1 s, and 4.2 s, is consistent with the fault surface being a nodal plane for the P-wave. Later, starting with time $t = 4.4$ s, we observe the development of a vertical offset at the location of the fault plane. This offset is the result of the vertical displacement carried by the rupture front which arrives at section A-A around $t = 4.4$ s. The vertical offset continues to develop in subsequent times ($t = 4.4$ s to $t = 4.6$ s) as the rupture tip propagates and the intense shock waves (Mach cones) cross section A-A at the location of the fault surface. This offset later disintegrates (\sim time $t = 5.2$ s and later) into a pair of waves propagating in opposite directions towards the sides of the bay. As the rupture tip moves past section A-A, the Mach cone fronts intersect section A-A at different points as they expand away from the fault plane ($x_2 = 0$), and we highlight the effect of the Mach fronts on the sea surface height by the red arrows between times $t = 4.5$ s and $t = 5.0$ s. A local trough (crest) develops in the sea surface profile over the left (right) sides of the bay. These start with an initially small amplitude (\sim $t = 4.4$ s) and continue to grow slowly afterwards (\sim up to $t = 5.0$ s). When the Mach cone fronts intersect with section A-A at the location of the slopes, the amplitude of the crest and the trough rapidly increase. The trough and the crest develop because of the horizontal displacements that are induced by the dynamic seafloor motion which cause

bathymetry deformation and subsequent vertical variation in the sea surface height as discussed in the main text. Initially (~ up to $t = 5.0$ s), the slopes of the bay experience small horizontal displacements. The source of these displacements is the dilatational wave field existing ahead of the rupture tip and the Mach fronts, as well as any shear or Rayleigh wavefields that have been generated during the early stages of the rupture nucleation and propagation before its transitioning into supershear. However, at later times ($t > 5.0$ s), the Mach cones arrive. The Mach cone fronts carry larger horizontal displacements leading to a rapid increase in the amplitude of the trough and crest (~ up to $t = 6.9$ s). Subsequently, as the Mach cones move away from sec A-A, the dynamic horizontal displacements decrease, and we observe a gradual reduction in the amplitude of the sea surface perturbations over the slope ($t = 7.2$ s and $t = 7.5$ s). The subsequent evolution of the different tsunami features at later times is detailed in the main text as part of the discussion that follows Figure 3.

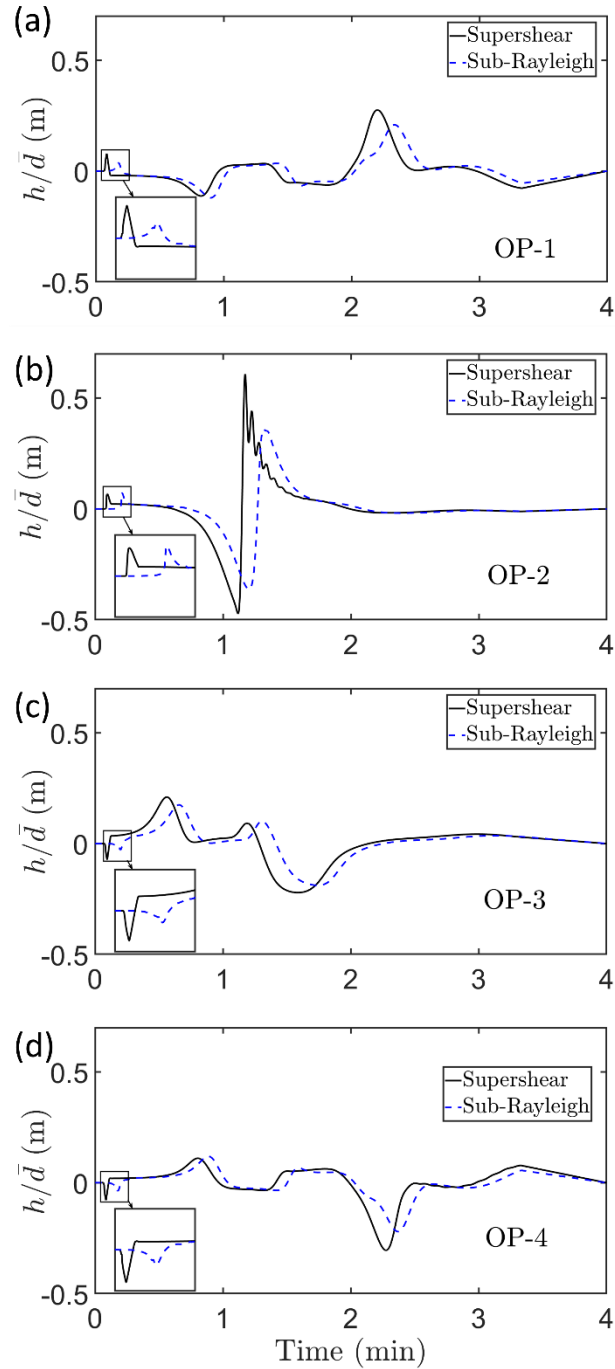


Fig. S4. Comparison between scaled water level time histories corresponding to a supershear and a sub-Rayleigh ruptures traversing the same bay. The water level is scaled by the average slip for each rupture scenario. The average slip for the supershear and the sub-Rayleigh cases is 3.6, and 2.25 m, respectively. The time histories are plotted for the tsunami at stations (a) OP-1, (b) OP-2, (c) OP-3, and (d) OS-4. Black solid lines correspond to water surface height associated with supershear rupture. Blue dashed lines correspond to water surface height associated with the sub-Rayleigh rupture. The arrival of the dynamic rupture-induced water wave is highlighted in the zoomed plot.

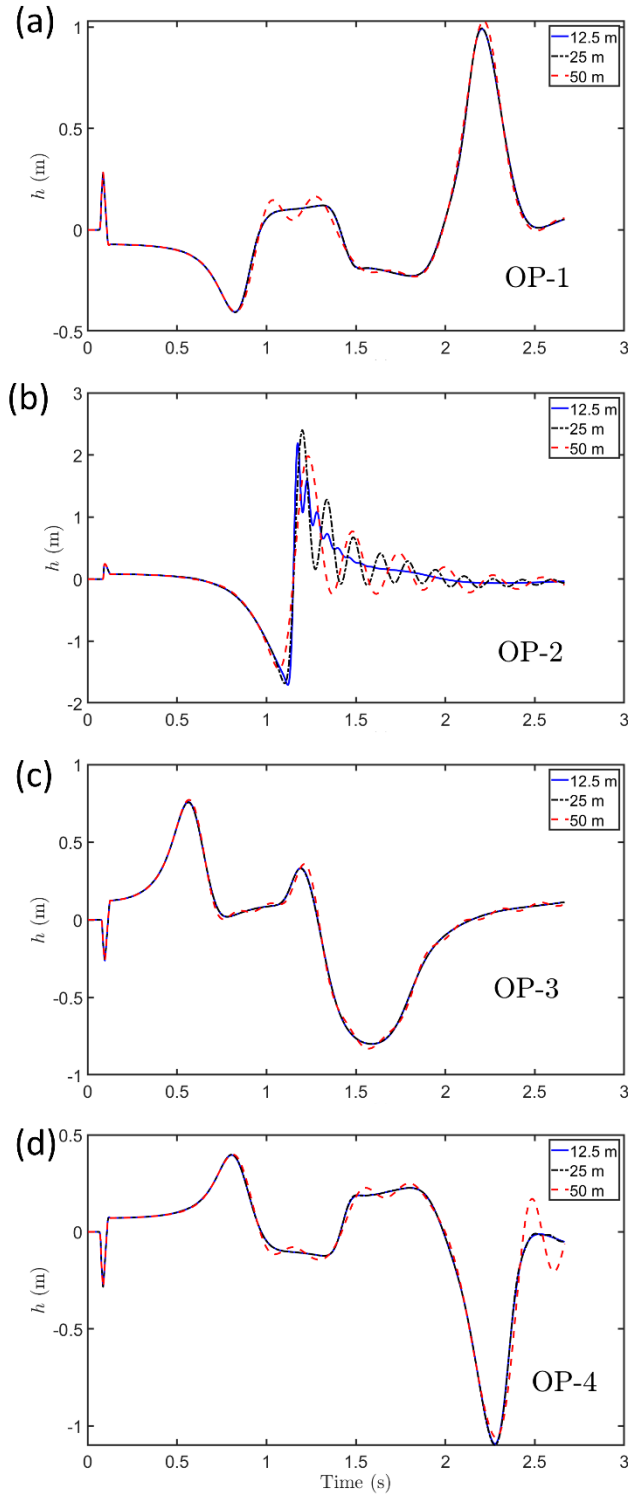


Fig. S5. Convergence of SWIM with mesh refinement. Three mesh resolutions are considered, with element sizes of 50, 25 and 12.5 m. The different plots show the time histories of the water level at the four different stations (a) OP-1, (b) OP-2, (c) OP-3, and (d) OP-4, identified in Fig. 2 in the main text. Across the three mesh resolutions, the results at stations OP-1, OP-3 and OP-4 converge and are virtually identical at mesh resolutions 25 m and 12.5 m. The amplitude and wavelength of the trailing oscillations observed in the water level at OP-2 are reduced when the mesh is refined. However, the peak amplitudes and wave arrival times do not change.

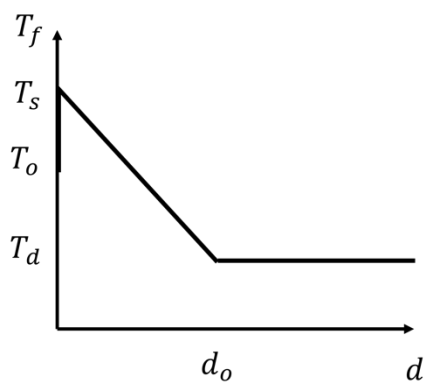


Fig. S6. A schematic of linear slip-weakening friction law showing the evolution of the frictional shear stress as a function of slip.

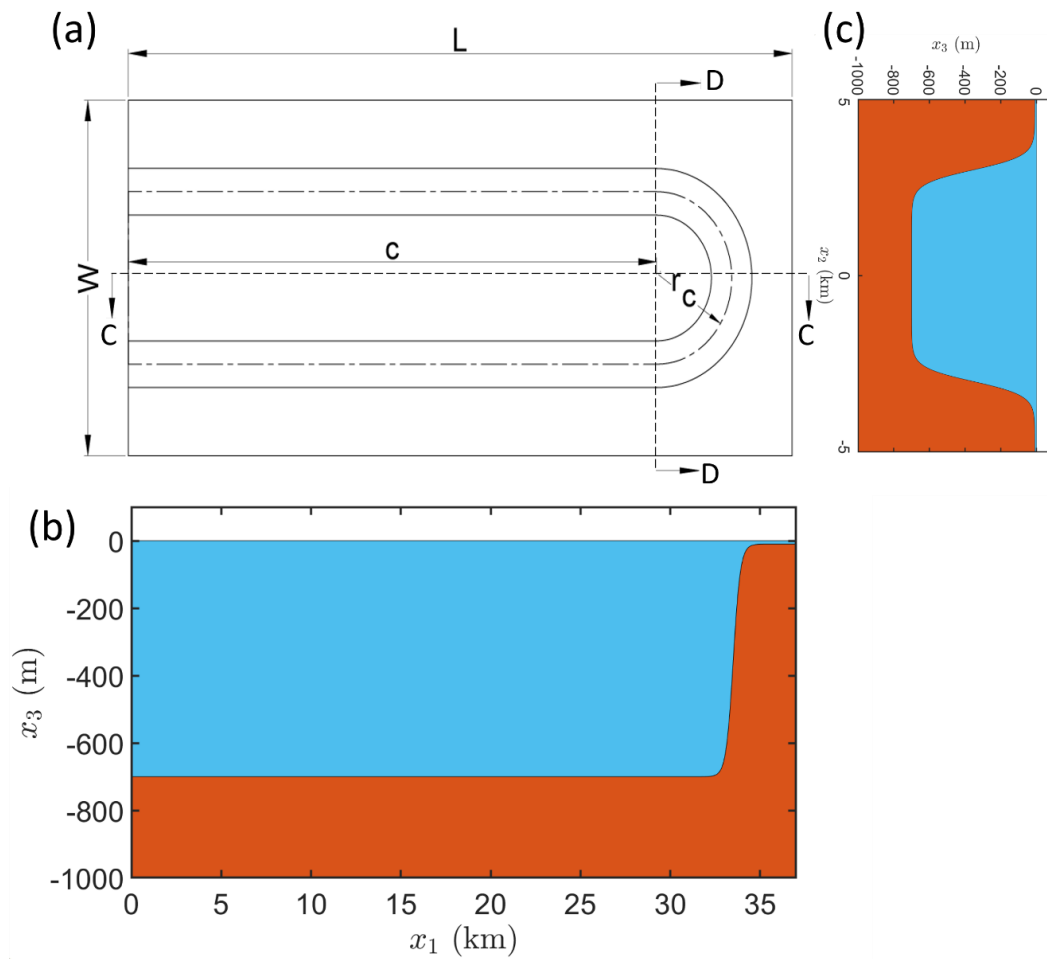


Fig. S7. Schematic of the bay geometry used in the tsunami model. (a) A plan view of the bathymetry. Here, L and W are the bay length and width respectively, c is the offset of apex center from $x_1 = 0$, and r_c is the mean radius of the apex; (b) Section C-C showing the water depth initial distribution along the strike-parallel direction at $x_2 = 0$; and (c) Section D-D showing the water depth initial distribution along the strike-normal direction at $x_1 = 0$.

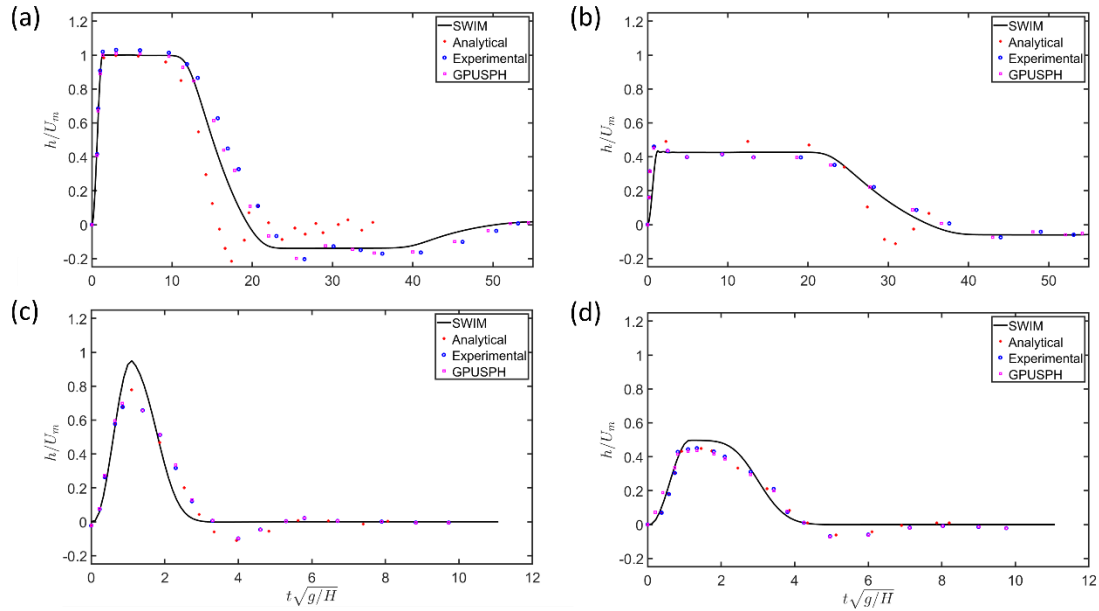


Fig. S8. Verification of SWIM solver using the benchmark problem in Derakhti et al. (2019). The numerical solutions of the nonlinear shallow water wave equation (NSWE) using SWIM is compared to experimental measurements, analytical estimates, and numerical solutions using the smoothed particle hydrodynamics (SPH) method as reported in Derakhti et al. (2019). The comparison shows the normalized time history of water surface level, h , for a punch, initially at rest at the sea floor and subsequently driven upward with hyperbolic cosine velocity profile. (a-b) Impulsive and (c-d) milder (transitional) time histories for bed displacements. The undisturbed water depth is H . Please see text in Section S3 for further explanation.

Table S1. Constitutive parameters for earthquake model

Medium Parameters	Value
Shear Modulus	32 GPa
S-wave velocity, c_s	3.464 km s ⁻¹
P-wave velocity, c_p	6 km s ⁻¹
Mass density	2670 kg m ⁻³

SI References

1. S. M. Day, L. A. Dalguer, N. Lapusta, Y. Liu, Comparison of finite difference and boundary integral solutions to three-dimensional spontaneous rupture. *J. Geophys. Res. Solid Earth* **110**, 1–23 (2005).
2. E. M. Dunham, Conditions governing the occurrence of supershear ruptures under slip-weakening friction. *J. Geophys. Res.* **112**, B07302 (2007).
3. Y. Kaneko, N. Lapusta, Supershear transition due to a free surface in 3-D simulations of spontaneous dynamic rupture on vertical strike-slip faults. *Tectonophysics* **493**, 272–284 (2010).
4. F. Hu, D. D. Oglesby, X. Chen, The Sustainability of Free-Surface-Induced Supershear Rupture on Strike-Slip Faults. *Geophys. Res. Lett.* **46**, 9537–9543 (2019).
5. M. Derakhti, R. A. Dalrymple, E. A. Okal, C. E. Synolakis, Temporal and Topographic Source Effects on Tsunami Generation. *J. Geophys. Res. Ocean.* **124**, 5270–5288 (2019).
6. R. A. Dalrymple, B. D. Rogers, Numerical modeling of water waves with the SPH method. *Coast. Eng.* **53**, 141–147 (2006).
7. J. L. Hammack, A note on tsunamis: Their generation and propagation in an ocean of uniform depth. *J. Fluid Mech.* **60**, 769–799 (1973).
8. T. S. Stefanakis, F. Dias, C. Synolakis, Tsunami Generation Above a Sill. *Pure Appl. Geophys.* **172**, 985–1002 (2015).